Supplementary material: Seasonal input and flux error results

We have used annual summary plots in the main text to summarize the various OSSE inputs and assimilation results. While this saves space, it masks the strong variations in both the input and output across the seasonal cycle. Here we give several multi-panel summary plots with this seasonal detail.

The single-sounding retrieval uncertainty patterns in Figs. S1a,b shift with the seasons as the SZAs shift north/south (Fig. 5a) and the median aerosol ODs (Fig. S1e) change with the seasons, particularly around the Sahara, the Middle East, central and east Asia, and certain ocean areas. The lowest single-sounding retrieval uncertainties are found over the high latitude oceans during winter in glint mode, where the high SZAs give the lowest ocean errors. However, the low path-length-corrected cloud free probability at these high SZAs (Fig. S2f) more than cancels out these lower values: the number of effective measurements per 1°x1° area (Fig. S2b) drops to its lowest values then due to difficulty finding cloud-free retrievals, and the resulting glint mode multi-sounding measurement uncertainties (Fig. S1d) are higher then than in the local summer. A SZA-dependent trend in the single-retrieval measurement uncertainties in the opposite direction occurs over the high-latitude northern land areas (lower uncertainties in the local summer), but because cloud effects do not dominate there, the multi-sounding measurement uncertainties remain lower in the local summer, in phase with the errors over the ocean. The lowest measurement uncertainties in both nadir and glint mode over land are achieved over dry areas that have low cloud amount while at the same time are not covered by thick aerosol layers: Australia, South Africa, and the northern Sahara, all in the local spring/summer.

These seasonal changes in the effective multi-sounding measurement uncertainties are convoluted with seasonal changes in the location of predominantly rising and subsiding air over the extratropical land and ocean areas to give the seasonal shifts in the 7-day flux error reductions in Fig. S5. In glint mode over the oceans, the largest reductions occur when the sun is highest overhead, mainly due to the SZA-dependent reduction in cloud-free availability (eq. (3)) we use here, giving lower effective measurement uncertainties. Figure S4 gives the seasonally-varying RMS 7-day flux errors from which the error reductions are computed. Because of the

strong variability in the prior-truth flux differences (with the greatest differences over the extratropical vegetated land areas during the growing season), there is also strong variability in the a posteriori flux errors: they are higher when the a priori errors are also higher, in keeping with the fractional error reductions being more constant. The seasonal mean flux errors given in Fig. S3 seem to show an opposite behavior, at least in the perfect model experiments, with the lowest errors occuring during the northern growing season and the largest biases occuring in the far north during local winter.

Figure S1: Seasonal averages (Jan-Mar, Apr-Jun, Jul-Sep, Oct-Dec) of: the single-sounding OCO X_{CO2} retrieval uncertainties σ_{1_shot} [ppm] for a) nadir and b) glint viewing modes; the effective multi-sounding OCO X_{CO2} uncertainty $\sigma_{eff} = \sigma_{1\_shot}/\sqrt{N_{eff}}$, at 1°x1° [ppm], for c) nadir and d) glint; e) the median aerosol OD at 760 nm (from Aqua/MODIS data); f) the assumed spatial representation error [ppm], extrapolated from Corbin, et al (2008); and the assumed measurement uncertainties [ppm] added to account for g) aerosol biases (Exps. 4 & 6) and h) transport errors (Exps. 5 & 6).

Figure S2: Seasonal averages (Jan-Mar, Apr-Jun, Jul-Sep, Oct-Dec) for: the effective number of independent X_{CO2} measurements N_{eff} across a single 1º latitude crossing for a) nadir and b) glint viewing modes; the pathlength-corrected probability P_{HiAeroOD} of encountering 760 nm aerosol ODs ≥0.30 (from Aqua/MODIS data) for c) nadir and d) glint; the path-corrected probability $P_{\text{cloud-free}}$ of finding at least one cloud-free X_{CO2} measurement across a ground track of length L (see Fig. 5b) (from MODIS data, see Appendix) for e) nadir and f) glint; g) the cloud-free probability at 1 km x 1 km (from the Aqua/MODIS Level 3 data cloud-mask product); and h) $P_{\text{cloud-free}}$ of from f) *before* path correction. Note: correlation length L is longer in glint mode than nadir, resulting in higher $P_{\text{cloud-free}}$ values; however, since a longer L also results in fewer potential independent retrievals per grid box, the N_{eff} ends up being lower in glint.

Figure S3: Seasonal mean flux errors [10^{-8} kgCO2 m^{-2} s^{-1}] (Jan-Mar, Apr-Jun, Jul-Sep, & Oct-Dec) after 50 minimization steps for experiments: a) #1 (Nadir, random errors only), b) #3 (Glint, mis-tuned), c) #2 (Glint, random errors only), d) #5 (Glint, random+transport errors), and e) #4 (Glint, random+aerosol bias errors), as well as f) the a priori flux errors.

Figure S4: RMS 7-day a posteriori CO_2 flux errors [10^{-8} kg CO_2 m^{-2} s^{-1}] for Jan.-March, April-June, July-Sept., and Oct.-Dec. after 50 minimization steps for experiments: a) #1, b) #3, c) #2, d) #5, and e) #4, as well as f) the a priori flux errors.

Figure S5: Fractional error reductions in 7-day CO_2 fluxes, computed across Jan.-March, April-June, July-Sept., and Oct.-Dec. from the RMS flux differences in Fig. S4 for experiments: a) #1, b) #3, c) #2, d) #5, e) #4, and f) #6 (Glint, Mis-tuned, Random+transport+aerosol bias errors).

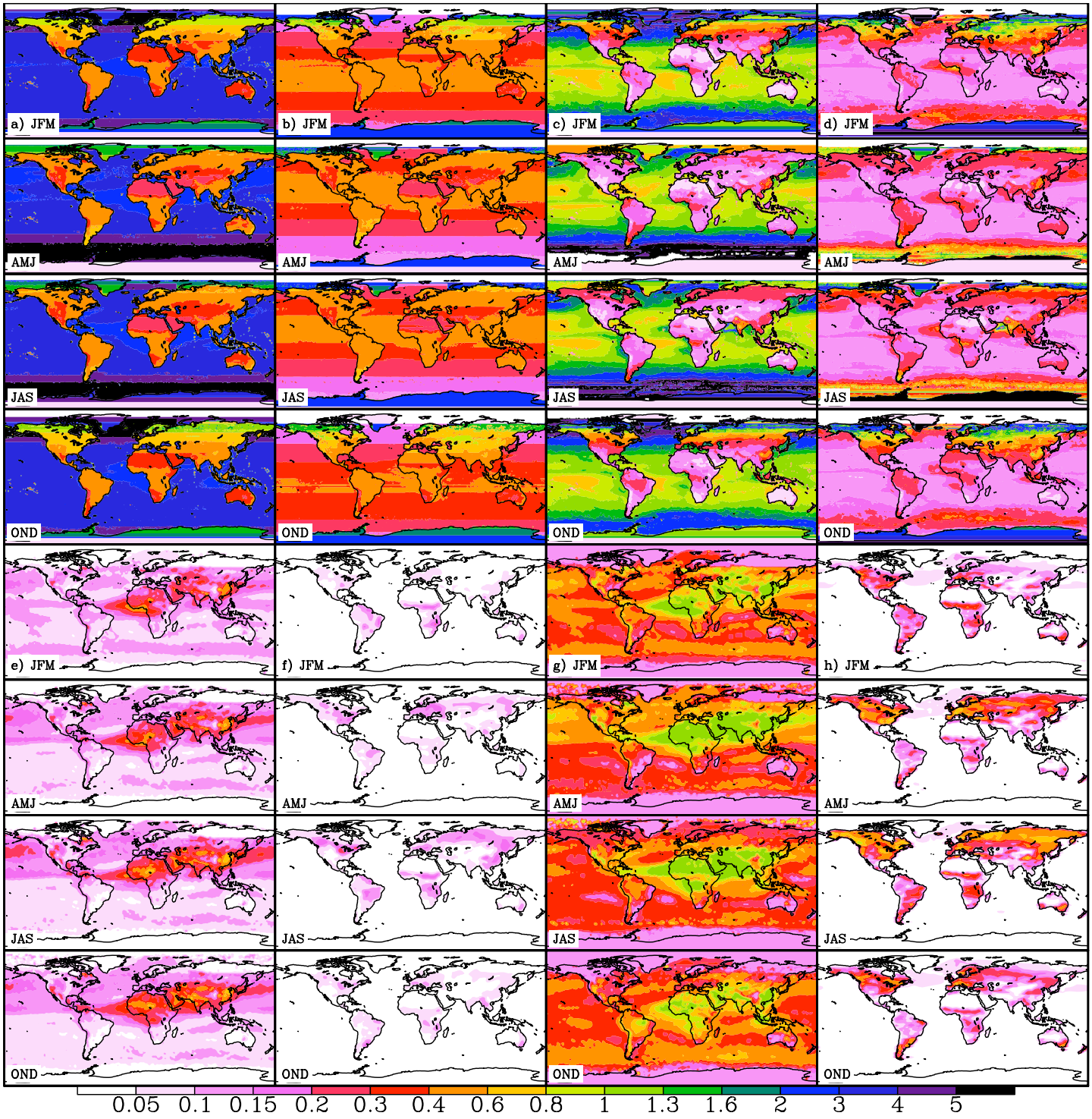

Figure S1: Seasonal averages (Jan-Mar, Apr-Jun, Jul-Sep, Oct-Dec) of: the single-sounding OCO X_{CO2} retrieval uncertainties σ_{1_shot} [ppm] for a) nadir and b) glint viewing modes; the effective multi-sounding OCO X_{CO2} uncertainty $\sigma_{eff} = \sigma_{1\_shot}/\sqrt{N_{eff}}$, at 1°x1° [ppm], for c) nadir and d) glint; e) the median aerosol OD at 760 nm (from Aqua/MODIS data); f) the assumed spatial representation error [ppm], extrapolated from Corbin, et al (2008); and the assumed measurement uncertainties [ppm] added to account for g) aerosol biases (Exps. 4 & 6) and h) transport errors (Exps. 5 & 6).

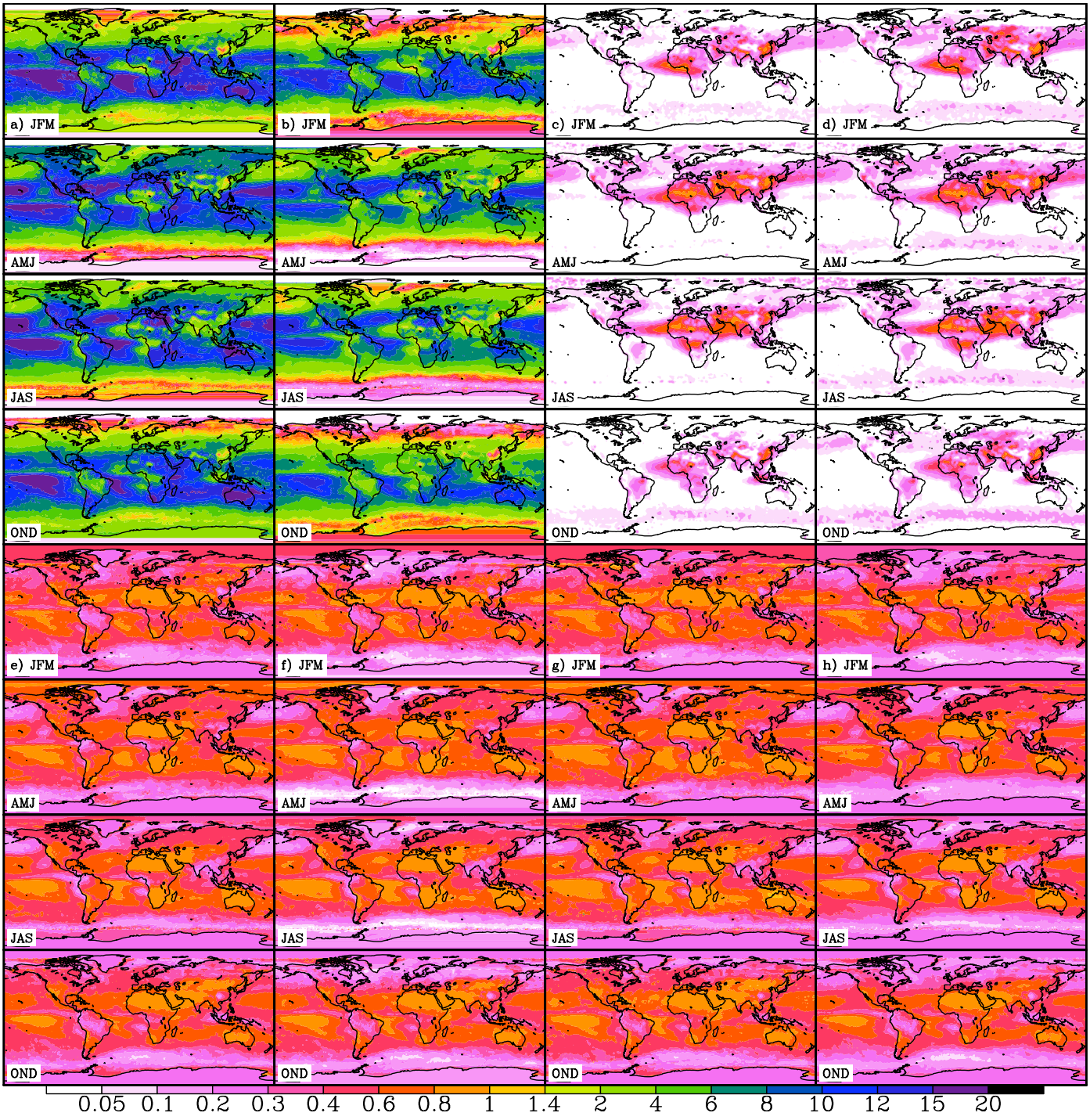

Figure S2: Seasonal averages (Jan-Mar, Apr-Jun, Jul-Sep, Oct-Dec) for: the effective number of independent X_{CO2} measurements N_{eff} across a single 1º latitude crossing for a) nadir and b) glint viewing modes; the pathlength-corrected probability P_{HiAeroOD} of encountering 760 nm aerosol ODs ≥0.30 (from Aqua/MODIS data) for c) nadir and d) glint; the path-corrected probability $P_{\text{cloud-free}}$ of finding at least one cloud-free X_{CO2} measurement across a ground track of length L (see Fig. 5b) (from MODIS data, see Appendix) for e) nadir and f) glint; g) the cloud-free probability at 1 km x 1 km (from the Aqua/MODIS Level 3 data cloud-mask product); and h) $P_{\text{cloud-free}}$ of from f) *before* path correction. Note: correlation length L is longer in glint mode than nadir, resulting in higher $P_{\text{cloud-free}}$ values; however, since a longer L also results in fewer potential independent retrievals per grid box, the N_{eff} ends up being lower in glint.

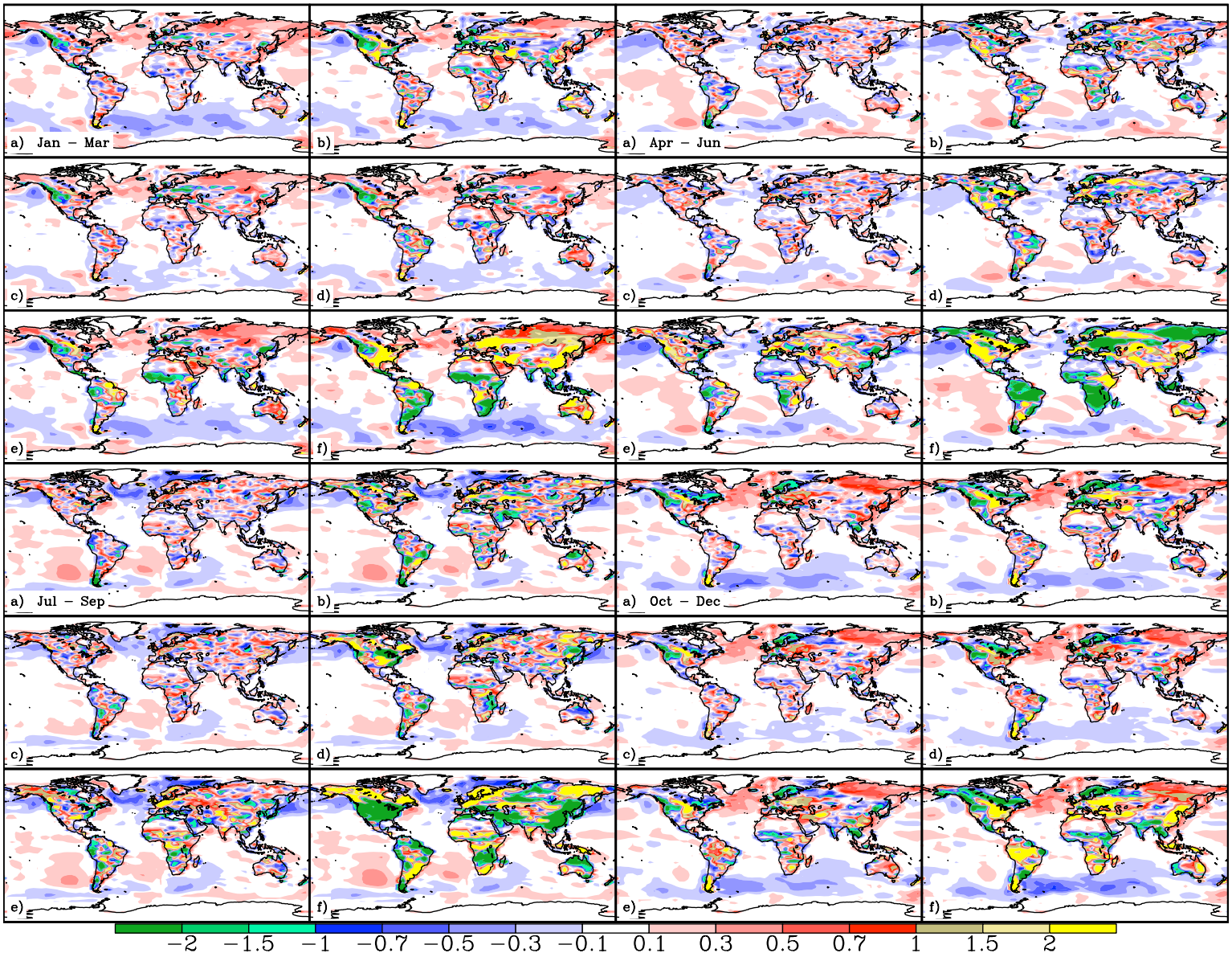

Figure S3: Seasonal mean flux errors [10^{-8} kgCO2 m^{-2} s^{-1}] (Jan-Mar, Apr-Jun, Jul-Sep, & Oct-Dec) after 50 minimization steps for experiments: a) #1 (Nadir, random errors only), b) #3 (Glint, mis-tuned), c) #2 (Glint, random errors only), d) #5 (Glint, random+transport errors), and e) #4 (Glint, random+aerosol bias errors), as well as f) the a priori flux errors.

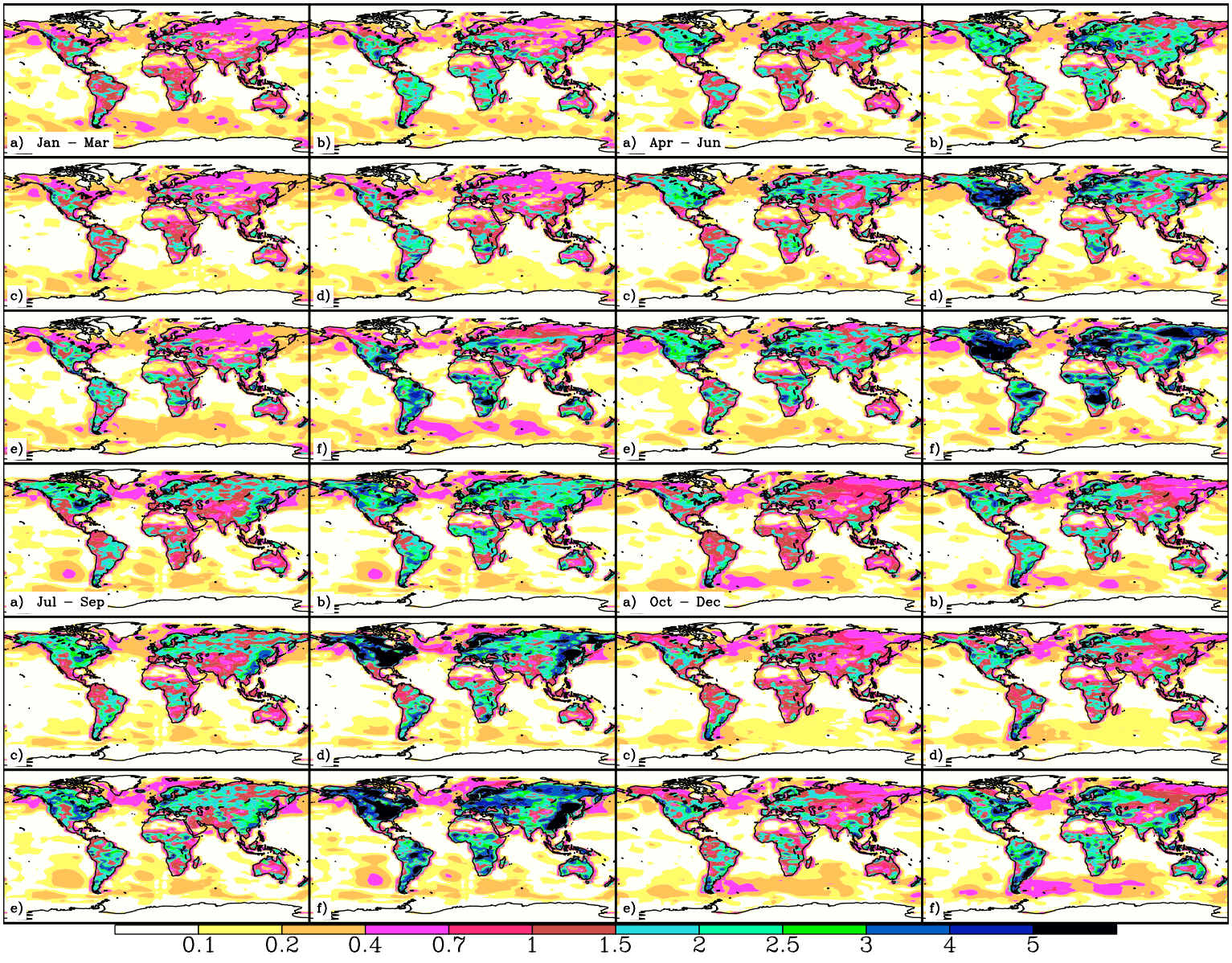

Figure S4: RMS 7-day a posteriori CO_2 flux errors [10^{-8} kg CO_2 m^{-2} s^{-1}] for Jan.-March, April-June, July-Sept., and Oct.-Dec. after 50 minimization steps for experiments: a) #1, b) #3, c) #2, d) #5, and e) #4, as well as f) the a priori flux errors.

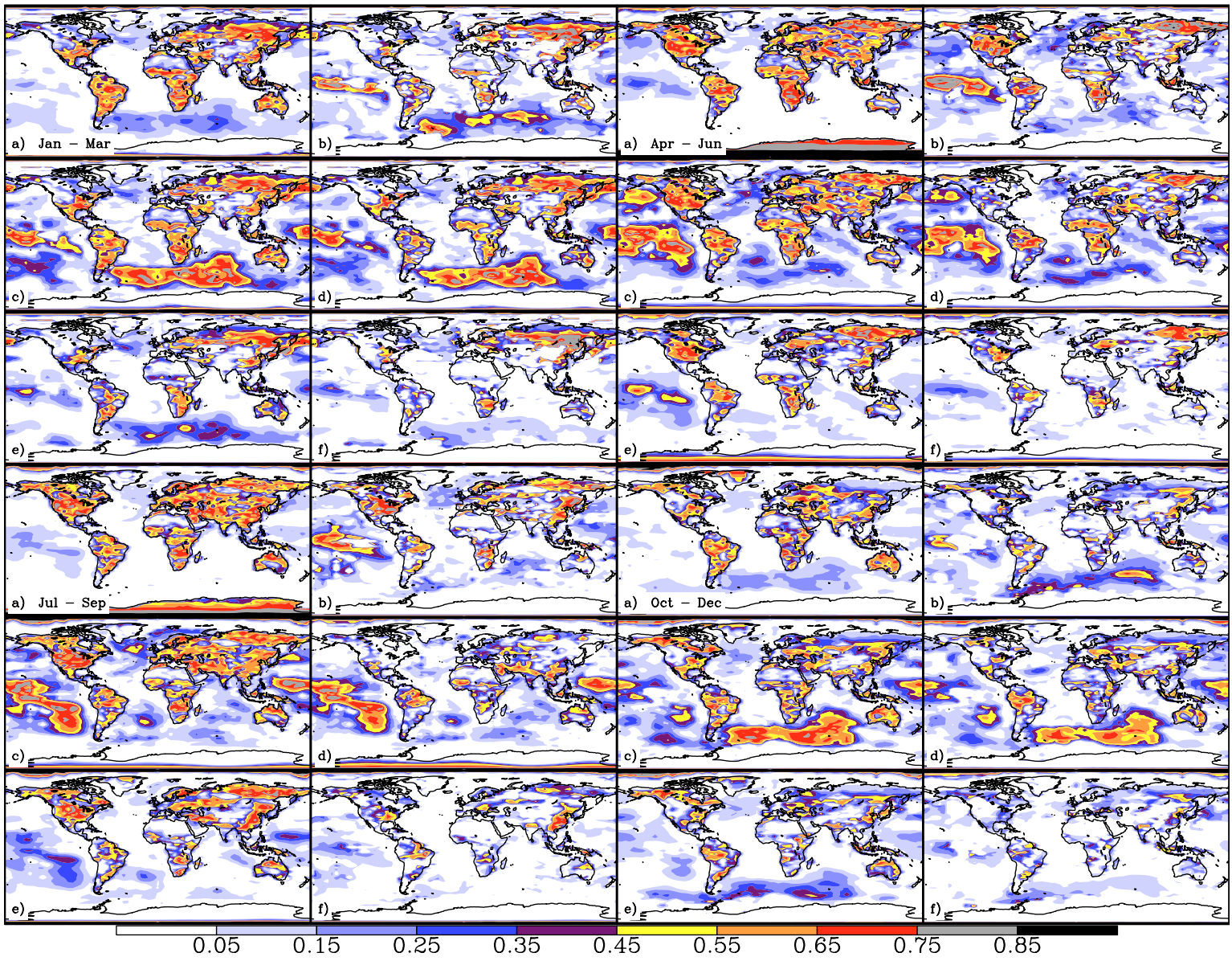

Figure S5: Fractional error reductions in 7-day CO_2 fluxes, computed across Jan.-March, April-June, July-Sept., and Oct.-Dec. from the RMS flux differences in Fig. S4 for experiments: a) #1, b) #3, c) #2, d) #5, e) #4, and f) #6 (Glint, Mis-tuned, Random+transport+aerosol bias errors).